Distributed Thermal Monitoring of Wind Turbine Power Electronic Modules Using FBG Sensing Technology

Anees Mohammed, Borong Hu, *Student Member, IEEE*, Zedong Hu, Siniša Djurović, *Member, IEEE*, Li Ran, *Senior Member, IEEE*, Mike Barnes, *Senior Member, IEEE*, and Philip A. Mawby, *Senior Member, IEEE*

Abstract—This paper reports a distributed thermal monitoring scheme for power electronic modules (PEMs) in wind turbine converters. The sensing system is based on utilizing electrically non-conductive and electromagnetic interference immune fiber Bragg Grating (FBG) sensing technology embedded in the PEM baseplate. The design and implementation features of the proposed scheme are presented first. The scheme is then applied in a commercial PEM operating within an inverter bridge, equipped also with a conventional distributed thermal monitoring system using a multiple point thermo-couple (TC) sensor suite. A range of tests are performed to evaluate the performance of the FBG distributed thermal monitoring system and correlate it to TC measurements under steady-state and transient operating conditions representative of PEM operation in an actual wind turbine application. It is shown that the proposed FBG monitoring system can offer practical operational improvements in establishment of distributed thermal sensing schemes for wind turbine PEM.

Index Terms— Power electronic module, temperature monitoring, distributing thermal sensing, fibre Bragg grating temperature sensors (FBG).
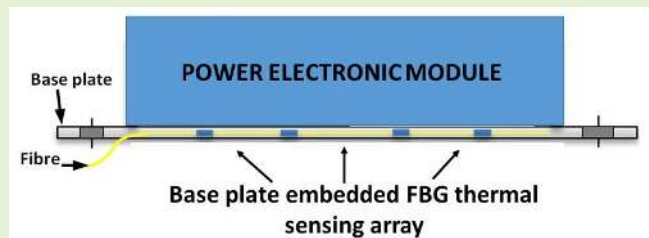
I. INTRODUCTION

POWER electronic modules such as insulated gate bipolar transistors (IGBTs) are a crucial power conversion and control component, widely used in consumer electronic devices and industry, including traction applications, renewable generators and grid control devices [1]. Wind turbines in particular work in complex operating, and extreme environmental, conditions, where due to a wide range of wind speed variation the turbine generator side power converter is typically utilized in a broad frequency band [2]. This can result in significant power electronic module (PEM) temperature swings, which, in combination with the mismatch in packaging material and chip coefficients of thermal expansion (CTE), can lead to considerable thermomechanical fatigue [3], [4].

Approximately 38% of faults in variable-speed ac drives are due to the failure of power devices [5]. Regarding wind turbine systems' overall annual failure rates, approximately 13% is attributed to frequency converter faults, which are second only to the pitch system failure rate (around 22%) [6]. Recent studies on some 35,000 turbine downtime events indicate that 18.4% of overall downtime hours lost were due to the frequency converter downtime [7].

An unpredicted power converter failure may trigger a catastrophic accident or unscheduled maintenance resulting in high cost repair and expensive downtime [8]–[10]. The development of effective diagnostic methods that can enable understanding and prediction of PEMs' health state is thus of considerable interest for maintaining wind turbine operational integrity. In principle, for diagnosis of the operational state, and thus health, of a power electronic device, information on its junction temperature is essential. This however is challenging to obtain, so the information on more readily accessible temperatures of its baseplate and cooling system is commonly

used to facilitate device health condition monitoring [11]. To this end, the available studies propose a large number of temperature sensitive electrical parameters to measure PEM device temperature indirectly [4]–[7]. Various researchers have recently explored health condition monitoring methods where chip to case thermal resistance, temperature gradient and heat flux were investigated to predict solder degradation, and thus the ageing level of the power module [12]–[14]. Effective online measurement of PEM's temperatures is shown to be key to its effective health monitoring but remains challenging due to device geometry and electromagnetic interference (EMI) rich operating environment [8].

Conventional temperature measurement sensors such as thermocouples (TCs), resistance temperature detectors (RTDs), platinum resistance thermometers (PRTs) and thermistors have a number of inherent limits for effective PEM temperature monitoring use [18]. This principally concerns the exposure to the high EMI environment inherent to PEM operation, which can affect TC readings by inducing voltage in its wiring and/or leading to inductive heating of the TC itself. RTDs on the other hand can provide high accuracy and have good immunity to electromagnetic fields. However, they tend to be large in size and are not always suitable for application in industrial environments. When a current flows through a thermistor, it generates heat, which raises the temperature of the thermistor above that of its environment. This electrical heating may introduce significant error if a correction is not made. In summary, electrically based temperature-sensing systems are generally impractical for application in PEMs, due to the presence of high EMI that can compromise measurement reliability. In addition, their large size and bulky wiring is detrimental to the compact structure of power electronic devices and can reduce the efficiency of heat transfer [16], [17].

As an alternative to conventional thermal sensing approaches, noncontact optical temperature sensors, such as infrared (IR) sensors, IR cameras and IR microscopes were also applied to capture PEM temperature [18]. However, these optical systems are not suitable for real time monitoring applications and are thus largely used for laboratory testing.

Optical fibre Bragg grating (FBG) sensing technology is fully immune to EMI, power passive, of small size, lightweight and flexible, and can be multiplexed to allow a single sensing fibre to carry an array of distributed sensing points. These are highly attractive sensing features that provide distinct advantages over conventional and non-contact sensing techniques. Consequently, the application of FBG technology for monitoring physical parameters in the power industry is increasingly developing as a promising alternative to more conventional techniques [19]–[26].

FBG sensing applications for PEM monitoring has only recently started to be explored, with a handful of studies suggesting encouraging potential for this application [17], [27]–[29]. Reference [18] proposes a general architecture of an FBG temperature sensing system that can be mounted at different PEM locations thermal monitoring. Reference [27] designed an FBG-bimetal temperature sensor to monitor IGBT case temperature in a solar panel inverter. Reference [28] explored the monitoring of IGBT junc-
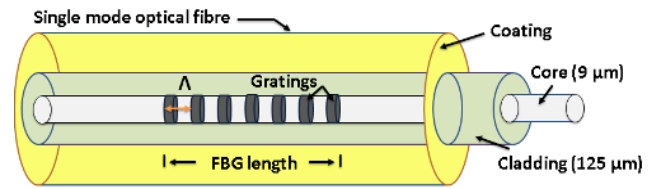

Fig. 1. FBG sensor structure.

tion temperature through application of direct FBG sensing. Reference [29] examines online temperature distribution monitoring of IGBTs by integrating FBG arrays into IGBT module silicone gel. The reported studies however focus on exploring invasive methods, whose application potential would be limited in in-service modules as it requires access to module internals and involves complicated and intrusive installation procedures.

This study aims to explore the potential of FBG array sensor application to improve current practices for distributed thermal monitoring in the PEM external structure (baseplate). The paper reports an experimental study that examines the design, implementation, characterisation and performance of an FBG array thermal sensor applied in the baseplate of a commercial PEM. A conventional distributed thermal monitoring system using a TC suite was also fitted on the test module. A range of tests in steady-state and transient conditions representative of PEM operation in an actual wind turbine application were undertaken to enable FGB versus conventional sensing performance comparison and cross-validation. The obtained experimental data show that the reported FBG sensing system can provide practical operational improvements in establishment of distributed thermal sensing schemes for wind turbine converters.

II. FBG SENSING TECHNOLOGY

Fig. 1 shows a schematic diagram of an FBG sensor architecture. The FBG sensor is a microstructure, typically a few millimeters in length, imprinted in the core of a single mode optical fibre. It is fabricated by exposure of a segment of the fiber's core to a pattern of UV light. This process induces a permanent physical change, creating a periodic modulated refractive index in the structure of the silica core [21].

The FBG sensing concept is based on light reflection capability and the modulated refractive index's sensitivity to variation of external thermal and/or mechanical conditions acting on the FBG structure [18]. In principle, the fibre carrying an FBG head is illuminated with broadband light; a narrow bandwidth of wavelength (i.e. that meets FBG Bragg conditions) will thus be reflected back by the FBG head. The reflected (Bragg) wavelength (λ_B) can be expressed as [24]:

$$\lambda_B = 2\Lambda n_{eff}, \tag{1}$$

where: Λ is the grating period and n_{eff} is the effective fibre core refractive index. These parameters can alter with a change in temperature and/or strain acting on an FBG, and consequently result in an alteration of the reflected Bragg wavelength, as demonstrated in Eq (1). Thus, monitoring the
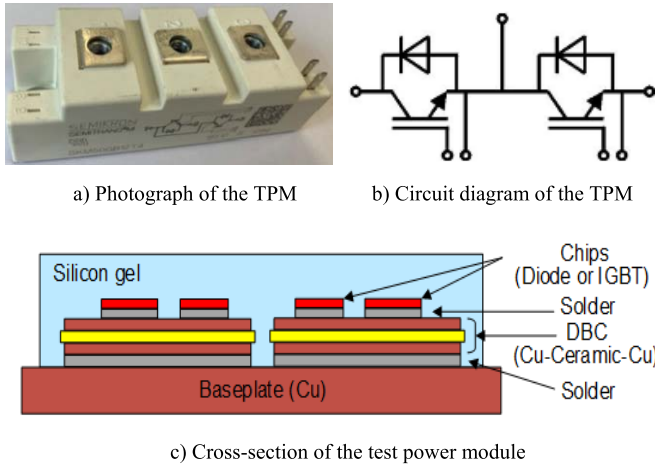
a) Photograph of the TPM b) Circuit diagram of the TPM

c) Cross-section of the test power module

Fig. 2. Test power module design.

TABLE I
SPECIFICATION OF TEST POWER MODULES

Parameters	Values	Unit
V_{CE}	1200	V
I_C	50	A
$T_{j,max}$	150	°C
$T_{j,min}$	-40	°C

FBG reflected Bragg wavelength shift can provide information on strain and temperate levels acting on its structure. With an appropriate FBG sensor design, exclusive temperature measurements can be obtained.

Assuming constant strain, the reflected wavelength shift variation due to temperature change can be expressed in terms of the fibre thermal characteristics as [25]:

$$\frac{\Delta \lambda_B}{\lambda_B} = (\frac{1}{\Lambda}\frac{d\Lambda}{dT} + \frac{1}{n_{eff}}\frac{dn_{eff}}{dT})\Delta T \qquad (2)$$

The first part of Eq (2) represents the change in Λ due to the fibre thermal expansion coefficient effect ($\approx 0.55 \times 10^{-6}/°C$). The second part of Eq. (2) represents the change in n_{eff} due to the fibre thermo-optic coefficient effect ($\approx 6 - 9 \times 10^{-6}/°C$) [24], [25]. Theoretically, for a bare FBG fabricated with a standard Bragg wavelength at 1550 nm, the temperature sensitivity can be evaluated to be $\approx 10 - 14$ pm/°C [19]. However, this value can vary with the FBG sensor packaging and instrumentation methods.

III. DESCRIPTION OF TEST SYSTEMS

This section describes the test system used in this study including: the test power module, the FBG thermal sensing system design, installation and thermal calibration procedures, and finally the test-rig system setup.

A. Test Power Module

The test power module (TPM) is a half bridge IGBT module (SKM50GB12T) manufactured by SEMIKRON with 1200V/50A rating. Fig. 2 shows a photo of the TPM (Fig. 2a), its circuit diagram (Fig. 2b) and structure (Fig. 2c). The module comprises two series connected IGBTs jointly forming an inverter leg section, each having a parallel freewheeling diode. The upper and the lower leg (one IGBT and one diode) are soldered by using SnAg3Cu0.5 (SAC305) solder paste on two direct bonded copper (DBCs) sections individually, as shown in Fig. 2c. Two DBC sections are made up of Cu/Al$_2$O$_3$/Cu and then soldered on one copper baseplate. This multi-layer structured packaging system is designed for both insulation

and cooling purposes. The PEM heat is generally dissipated to the ambient from the top (IGBTs and diodes), drawn to the base, and then on to the cooling system.

Table I presents the specifications of the TPM: each IGBT and diode device has the capability of blocking 1200 V (V_{CE} = 1200 V) or conducting 50 A (I_C = 50 A) current continuously. The junction temperature (T_j) of a semiconductor chip is usually determined by the nature of silicon material. According to product specification given by the manufacturer, the devices' operating junction temperature range is limited to a minimum of −40 °C and a maximum of 150 °C.

B. Proposed FBG Temperature Sensing System

1) FBG Thermal Sensor Design: The proposed FBG thermal sensor was designed and prototyped based on the TPM architecture. The target sensing application in this study is distributed temperature sensing in the baseplate of the TPM. To this end, an FBG array sensor with four FBG heads imprinted in a polyimide coated single-mode optical fiber was designed and prototyped. Polyamide fiber was chosen for this application due to its high temperature resistance (up to ≈300 °C).

Fig. 3a illustrates the FBG array sensor architecture; it consists of four 5mm long FBG heads with an average bandwidth of ≈0.3 nm and reflectivity of ≈80 %. The sensing heads were distributed along the fibre based on the TPM's chip architecture. The spacing was designed to ensure that each sensing point (FBG head) in the array installed in its baseplate is located vertically under a target chip. For illustration, Fig. 3b shows the thermal sensing points distribution in the baseplate considering the chips' positions in the TPM. The FBG head locations are seen to be designed to mirror individual chip positions and are named accordingly as follows: FBG-IG1 (for IGBT1), FBG-D1 (for diode1), FBG-IG2 (for IGBT2) and FBG-D2 (for diode2).

To eliminate mechanical excitation (strain) effects on array FBGs' Bragg wavelength shift, which may induce error in the thermal measurements due to FBG inherent thermo-mechanical cross-sensitivity, the fibre section containing the FBG heads is loosely packaged within a brass capillary. The remainder of the optic cable is Teflon tubed for protective purposes. The brass capillary is integrated into the TPM baseplate, to allow precision placement of array sensor's individual sensing heads but also to ensure sensor protection during installation. The chosen capillary dimensions are 0.3 mm inner diameter and 0.5 mm outer diameter. This ensures a sufficient air-gap to house the sensing fiber in its
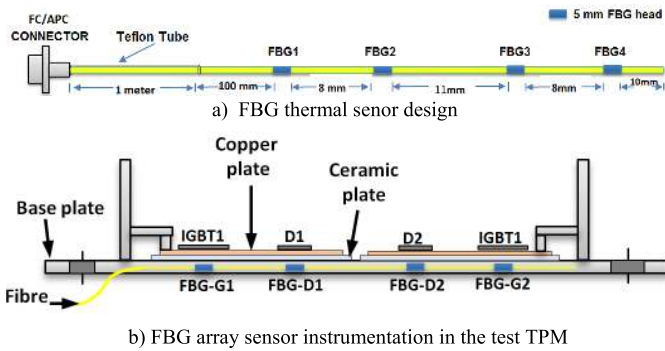
a) FBG thermal senor design

b) FBG array sensor instrumentation in the test TPM

Fig. 3. FBG array sensor design and instrumentation.

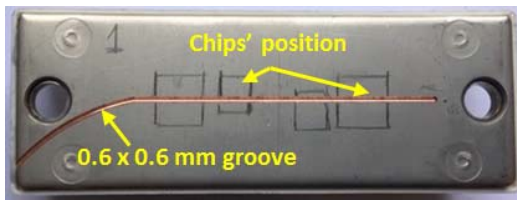Fig. 5. FBG array thermal calibration.

Fig. 4. Grooved TPM.

bore, but also a fine wall thickness of ≈ 0.1 mm to enhance the sensor thermal response [21].

2) FBG Array Installation: The procedure of TPM instrumentation with the FBG array thermal sensor was conducted in following steps:

- First, a 0.6 x 0.6 mm groove was machined in the TPM baseplate along its axial centerline in the area beneath the known locations of the module chips where thermal hotspots are expected; at one groove side an exit curvature was made. This allows embedment of the packaging capillary into the TPM baseplate structure without interfering with the module mounting points and enables the sensing fibre to effectively interface with an external interrogator device. Fig. 4 shows an image of the grooved power module.

- The packaging brass capillary was then prepared with a length equal to that of the machined baseplate groove plus an additional few mms to enable sensing fibre insertion and the integration between the brass and Teflon packaging into a joint protective structure. Once prepared, the capillary was fitted into the groove using a thermally conductive adhesive (acrylic thermal adhesive).

- Finally, the FBG sensing array was carefully inserted into the capillary in the desired position. Heat shrink tubing was used to bond the brass and Teflon packaging.

The described process enables practical installation of a packaged FBG array sensor into a power module. The process makes the array sensor accessible for in-situ replacement or re-calibration, as well as effective re-positioning of sensing points for greater accuracy or coverage of additional locations of interest.

3) In-Situ FBG Thermal Calibration Procedure: The FBG array thermal sensor was thermally calibrated using a thermal chamber to obtain the appropriate wavelength shift-temperature fit curve for each FBG head. The FBG
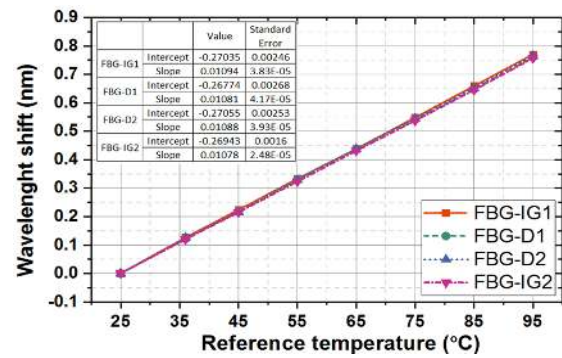
instrumented TPM was placed inside the thermal chamber and exposed to different levels of static thermal excitation from 25 °C to 95 °C in 10 °C increments. The FBGs' wavelength shifts were recorded at each applied temperature level using a temperature reference obtained from the thermal chamber readings. Fig. 5 shows the obtained calibration test data. The average temperature sensitivity of the FBG array sensor calculated from the slope of the calibration data linear fits was found to be ≈ 10.9 pm/°C. This value closely matches the theoretical calculated temperature sensitivity range of a bare FBG, demonstrating that the proposed packaging and installation procedure has a minimal effect on the array sensor.

C. Test-Rig Description

To evaluate the performance of the proposed thermal sensing system, the FBG array embedded TPM was operated in a back-to-back half bridge inverter test rig. The schematic diagram of the inverter rig with inductive load is shown in Fig. 6a. Module 1, highlighted by the red dotted line in the figure, is the FBG enabled TPM.

Fig. 6b shows the used test rig setup. The inductor load is connected between the AC terminals of the half-bridge modules and the neutral point of the DC-link comprises two series connected capacitors (HCGF6A, 15000 μF/ 450 V). The DC-link voltage is controlled at 200 V by a DC power supply (SL400, Magna Power). During the tests the power modules are controlled by the SKHI 23/12R gate driver with a PWM signal generated on a dSPACE RTS 1103 platform at a switching frequency of 2550 Hz. In this study the fundamental frequency of AC current through the inductive load is maintained at 50 Hz by employing a control loop embedded in Simulink/dSPACE. For cooling purposes, the power modules were placed on a water cooling heatsink (Hi-Contact 416601U) connected to an external chiller (Lauda WK4600).

The load current was measured in the tests by current probes (Pico TA167). A set of type K thermocouples (1/0.2mm diameter) was installed on the test rig, as shown in Fig. 7. Four TCs were located on the heat sink top in the area beneath the known locations of the module chips (T_{c1}-T_{c4} in Fig. 7, which correspond to the four thermal sensing points of the FBG array sensor installed in the baseplate). The heatsink inlet and outlet temperatures were measured by two TCs. Care was taken in TC installation and output signal conditioning to mitigate
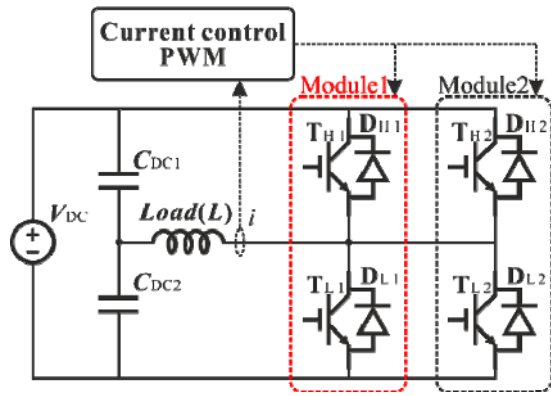
a) Schematic diagram of a back to back half bridge inverter circuit
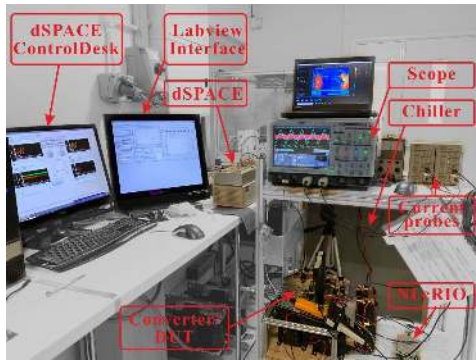
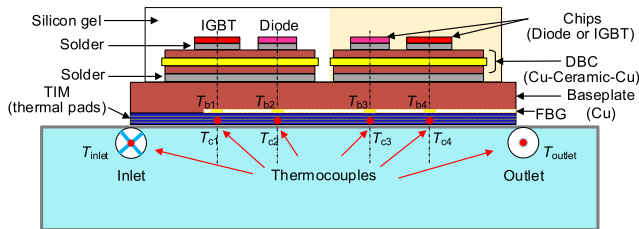(b) Photo of actual test rig

Fig. 6. Test rig setup.

Fig. 7. Schematic diagram of the two power modules locating on heatsink and 8 temperature measuring points' locations.

measurement error due to EMI, vibrations and voltage induced in the wiring as much as possible. The TC thermal sensing system was fitted on the test rig to enable cross-correlation and comparison with the readings provided by the proposed FBG sensing system.

To operate the FBG array sensor and obtain real-time temperature measurements, a commercial interrogator unit (SmartScan) was connected to it. The interrogator illuminates the array sensor using a broadband light source and receives the FBG reflected light. The monitored FBG wavelengths were processed and converted to temperature measurements using LabVIEW based SmartSoft software. The FBG measurements are sampled in this study at a rate of 2.5 kHz and the TC readings sample rate is 1 Hz.

IV. RESULTS AND DISCUSSION

This section reports the results of the experimental study undertaken to evaluate the application of the proposed thermal
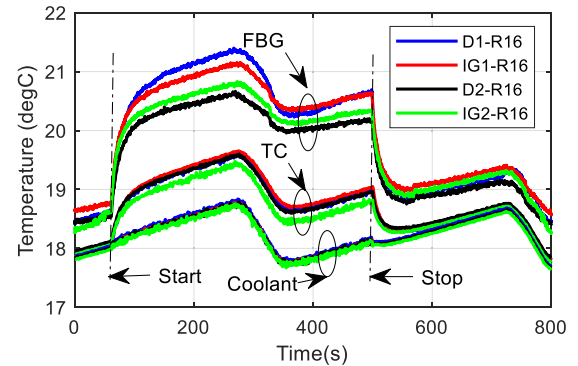
(a) Load current 10 A
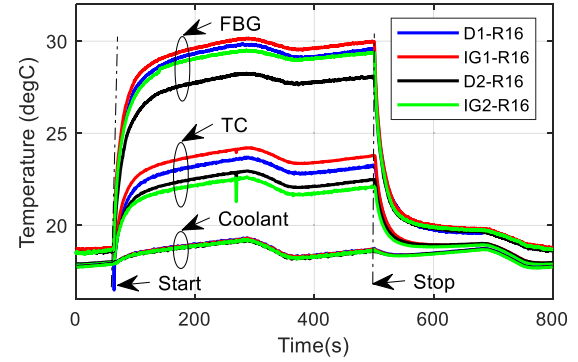
(b) Load current 50 A

Fig. 8. FBG and TC temperature measurements under static conditions.

monitoring scheme for power module thermal condition monitoring.

To examine the performance of the FBG based thermal sensing system, the inverter test rig was controlled to operate in both static and dynamic thermal states. For the static thermal conditions, different tests with different constant levels of load current were examined. Each static load current test starts from ambient temperature and lasts until the PEM thermal equilibrium is reached. The dynamic thermal conditions tests are performed for a variable load current profile that replicates load variability encountered in field inverters operating under a typical wind speed profile.

The obtained results are presented and discussed in the following subsections. Section A focuses on exploring the FBG thermal sensing system performance and cross-correlating it with conventional TC measurements under static thermal conditions. Section B undertakes validation of FBG in-situ thermal measurement against those provided by the TCs based on utilizing a thermal network model that allows their direct correlation. Finally, section C presents the results of examining the FBG sensing system response under a typical wind speed load profile.

A. Static Thermal Conditions

The static test results are presented in this section. These were undertaken on the test rig in the following uniformly distributed range of load current within the TPM nominal range: 10A, 20A, 30A, 40A and 50A. For illustration purposes, Fig. 8 shows the temperature measurements obtained by the

FBG array and TCs in the half bridge inverter test rig when operated under low and high load currents (10A and 50A).

The first 60s of data in Fig. 8 are measured with the test inverter not energized and the heatsink temperature controlled at ≈18 °C by the water-cooling chiller. As the TCs are fitted to the heatsink, their measurements are similar to the coolant temperature at ≈18 °C. The FBGs embedded within the TPM baseplate measure a temperature that is ≈0.6 °C higher than that of the coolant. This is due to FBGs not being in direct contact with the heatsink and the test room ambient temperature during test of ≈25 °C contributing to the temperature gradient from external ambient down to cooling system. Some discrepancy can be observed between trends reported by FBG and TC sensors which is believed to originate from challenges with ensuring optimal thermal contact during TC installation.

The converter is energized at the 60s point in tests and the thermal responses from both FBGs and TCs then observed during the step transient and the steady-state stage. As expected, due to their location and effective integration into the TPM structure, the FBGs recorded higher temperatures than the TCs. The temperature difference between FBGs and TCs is seen to increase with the increase of operating stress (≈1.5°C @ 10A and ≈6°C @ 50A), which indicates that FBGs obtained more thermal information from the TPM than the conventional TCs attached on the heatsink. The differences between individual FBG thermal readings in steady-state and step transient conditions is due to the heatsink temperature gradient due to the water cooling flow cycle. The general fluctuation in the thermal recordings is induced by the cooling capability thermal-inertia limitations of the chiller system used. The inverter is stopped at 500 s, resulting in a relatively rapid heat decrease whose dynamics are determined by the thermal inertia of the whole system, including the heat sink and the cooling chiller.

B. FBGs Thermal Measurement Validation

The TC measurements obtained cannot be directly used to validate the FBG thermal sensing system measurements. This is due to inherent installation limitations of the TCs, which are fitted in the top of the heat sink and not in the baseplate. This section presents a validation method of the FBG thermal measurements based on a thermal network model of the TPM and TC temperature measurements.

Fig. 9 shows the TPM thermal network schematic including the thermal pad and the water-cooled heatsink. The power loss is dissipated from the semiconductors (top of the module) to the heatsink and then to the ambient, forming a thermal path involving the following elements: $R_{th,j-c}$ is the junction to case thermal resistance of the power module, $R_{th,TIM}$ is the thermal resistance of the thermal pad as the thermal interface material (TIM), and $R_{th,hs}$ is the thermal resistance of the heat sink. The temperature measurement by FBG/ TC and coolant temperature are also illustrated in this diagram. It can be noted from the thermal model that the thermal resistance of the thermal pad, $R_{th,TIM}$, is the root cause of temperature measurement difference between the FBG and TCs. From the
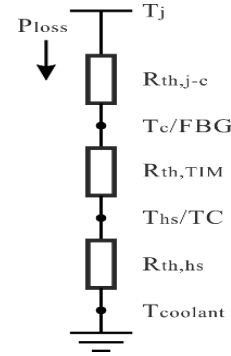

Fig. 9. Test power module thermal network.

TABLE II
THERMAL PAD PARAMETERS

Property	Value
Thickness (mm) (L)	0.5
Area (mm²) (A)	34 x 94
Thermal conductivity (W/(m·K)) (λ)	4

thermal model, $R_{th,TIM}$ can be derived from the power losses of the power devices and the temperature gradient between FBG (base temperature) and TCs (top heat sink temperature), Eq (3).

$$R_{th,TIM} = \frac{T_{Base} - T_{heatsink(top)}}{P_{loss}} \quad (3)$$

By comparing the derived thermal resistance from the thermal model given by Eq (3) and its nominal value deduced from the material properties and the geometry of the thermal pads, the FBG thermal measurements can be validated. The thermal resistance $R_{th,TIM}$ based on the material properties and geometry can be expressed as:

$$R_{th,TIM} = \frac{L}{A * \lambda} \quad (4)$$

where: L is the thickness of the thermal pad, A is the area and λ is the thermal conductivity of the TIM material. Detailed parameters of applied thermal pads are given in Table II. Using Eq (4) and Table I, the nominal thermal resistance $R_{th,TIM}$ of ≈0.1956 °C/W is obtained.

To analytically determine $R_{th,TIM}$ from the thermal model using Eq. (3), the power loss heat transferred through the system needs to be calculated. Here, the power losses are calculated based on the method [30] using test voltage/current measurements. The temperature dependent on-state and switching losses are extracted from the datasheet and then imported into an electrical-thermal model with the coolant temperature as ambient reference to derive the total power losses of each semiconductor. The calculated power losses for the 10A and 50A steps are shown in Fig. 10. The $R_{th,TIM}$ value was obtained using the calculated power loss and the temperature measurements from the FBGs and the corresponding TCs in the heatsink during the steady-state condition (from 350s to 500s in Fig. 8) examined in the previous section for 10 and 50 A tests. Fig. 11 shows the determined $R_{th,TIM}$ together with its nominal value calculated
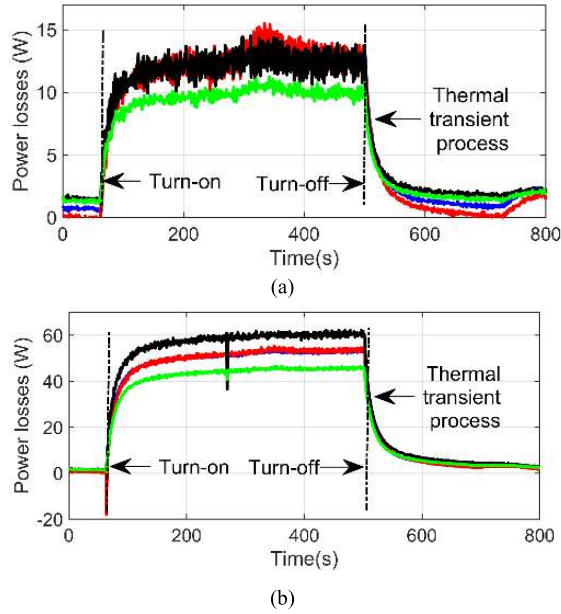
Fig. 10. Power losses calculation under (a) 10A and (b) 50A total current step-change conditions.
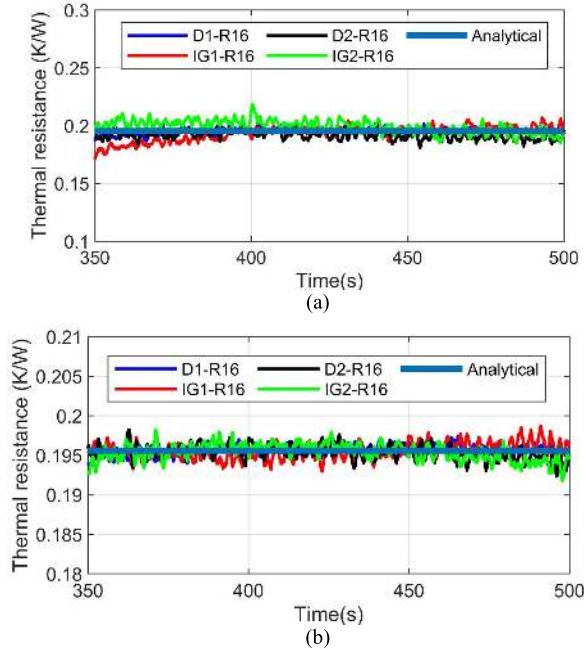

Fig. 11. Validation of temperature measurement based on thermal resistance of TIM, $R_{th,TIM}$, under: (a) 10A and (b) 50A total current conditions.

from Eq. (4) for all considered sensing locations. The results show the analytically calculated $R_{th,TIM}$ value matches its calculated nominal value, thus validating the FBG array sensor temperature measurements.

C. Dynamic Thermal Conditions

The dynamic response of the FBG array thermal sensor under transient thermal conditions is examined in this section. A wind speed representative dynamic load profile was applied

TABLE III
WIND PROFILE REPRESENTATIVE CONDITION

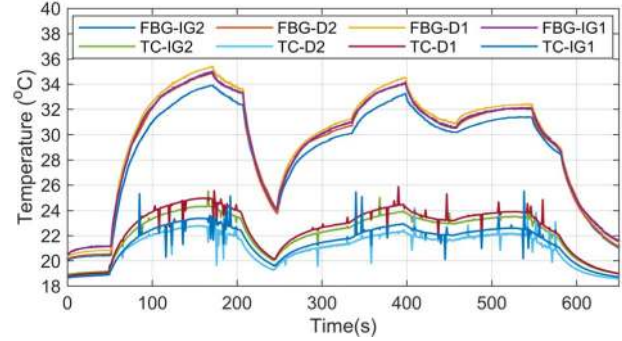| Time (s)	Current (A)	Time (s)	Current (A)
$0 - 50$	0	$340 - 400$	39.58
$50 - 170$	40.15	$400 - 460$	25.21
$170 - 200$	26.54	$460 - 550$	32.23
$200 - 250$	0	$550 - 580$	18.32
$250 - 340$	32.15	$580 - 650$	0

Fig. 12. Thermal measurement under dynamic condition.

on the test inverter, which was achieved by appropriate control of the inverter load current. Fig. 12 shows the recorded thermal measurements under the applied typical wind speed profile, comprising nine distinct load changes in the examined 650 period, as detailed in Table III.

The thermal measurements obtained by the FBGs show a higher sensitivity to dynamic thermal variation when compared with the TC measurements. The FBGs clearly registered the instant of change between steps, whereas the TC measurements were smooth and less detailed; the FBGs also recorded higher levels of thermal variation. For instance, FBG sensors recorded a temperature rise of ≈ 14 °C in the 1st step (current change from 0 to 40.15A) and a temperature drop of ≈ 9 °C in the 3rd step change (current change from 26.54 A to 0 A) – the corresponding TC measurements are an ≈ 6 °C temperature rise and a ≈ 3 °C temperature drop. Fig. 12 also demonstrates an important functional feature of FBG, which is EMI immunity: while the TC recordings are noisy and contain considerable temperature spikes, the FBG measurements are clear and unaffected by EMI.

V. CONCLUSIONS

This paper reports a study of fibre optic FBG distributed thermal sensing application for wind turbine and general power electronic device thermal monitoring. The sensor design, implementation and calibration principles are presented and an extensive experimental study is then undertaken to evaluate and validate the potential of the proposed sensing scheme in steady-state and transient conditions.

The findings demonstrate that the reported technique provides clear functional advantages compared to current distributed thermal monitoring practices for power electronic modules based on the utilisation of conventional thermal

sensors. Application of the proposed array sensing scheme enables effective distributed thermal sensing within the module baseplate using a single sensing optical fibre contained in a thermally conductive packaging, seamlessly integrated into the target monitoring area. The resulting thermal monitoring system is of considerably lower wiring and installation complexity in comparison to those employing conventional sensing techniques, and offers important advantages of full EMI immunity as well as ease of in-situ replacement or repositioning of the sensor array. These features allow the ability to improve the density and quality of the harvested thermal data and design much improved distributed thermal monitoring schemes compared to current general practices.

REFERENCES

[1] M. Liserre, R. Cardenas, M. Molinas, and J. Rodriguez, "Overview of multi-MW wind turbines and wind parks," *IEEE Trans. Ind. Electron.*, vol. 58, no. 4, pp. 1081–1095, Apr. 2011.

[2] L. Ran, D. Xiang, P. Tavner, and S. Yang, "Control of a doubly fed induction generator in a wind turbine during grid fault ride-through," *IEEE Trans. Energy Convers.*, vol. 21, no. 3, pp. 652–662, Sep. 2006.

[3] S. Yang, D. Xiang, A. Bryant, P. Mawby, L. Ran, and P. Tavner, "Condition monitoring for device reliability in power electronic converters: A review," *IEEE Trans. Power Electron.*, vol. 25, no. 11, pp. 2734–2752, Nov. 2010.

[4] M. Ciappa, "Selected failure mechanisms of modern power modules," *Microelectron. Rel.*, vol. 42, nos. 4–5, pp. 653–667, Apr. 2002.

[5] F. W. Fuchs, "Some diagnosis methods for voltage source inverters in variable speed drives with induction machines—A survey," in *Proc. 29th Annu. Conf. IEEE Ind. Electron. Soc.*, Nov. 2003, pp. 1378–1385.

[6] P. Tavner, "How are we going to make offshore wind farms more reliable?" *Supergen Wind*, to be published.

[7] H. Huang *et al.*, "Transitioning to physics-of-failure as a reliability driver in power electronics," *IEEE J. Emerg. Sel. Topics Power Electron.*, vol. 2, no. 1, pp. 97–114, Mar. 2014.

[8] L. Ran, P. Mawby, P. McKeever, and S. Konaklieva, "Condition monitoring of power electronics for offshore wind," *Eng. Technol. Reference*, vol. 1, no. 1, pp. 1–10, Jan. 2014.

[9] W. Lai, M. Chen, L. Ran, O. Alatise, S. Xu, and P. Mawby, "Low ΔT_j stress cycle effect in IGBT power module die-attach lifetime modeling," *IEEE Trans. Power Electron.*, vol. 31, no. 9, pp. 6575–6585, Sep. 2016.

[10] B. Hu *et al.*, "Failure and reliability analysis of a SiC power module based on stress comparison to a Si device," *IEEE Trans. Device Mater. Rel.*, vol. 17, no. 4, pp. 727–737, Dec. 2017, doi: 10.1109/TDMR.2017.2766692.

[11] D. Xiang, L. Ran, P. Tavner, S. Yang, A. Bryant, and P. Mawby, "Condition monitoring power module solder fatigue using inverter harmonic identification," *IEEE Trans. Power Electron.*, vol. 27, no. 1, pp. 235–247, Jan. 2012.

[12] D. Xiang, L. Ran, P. Tavner, A. Bryant, S. Yang, and P. Mawby, "Monitoring solder fatigue in a power module using Case-Above-Ambient temperature rise," *IEEE Trans. Ind. Appl.*, vol. 47, no. 6, pp. 2578–2591, Nov. 2011, doi: 10.1109/TIA.2011.2168556.

[13] B. Gao *et al.*, "A temperature gradient-based potential defects identification method for IGBT module," *IEEE Trans. Power Electron.*, vol. 32, no. 3, pp. 2227–2242, Mar. 2017, doi: 10.1109/tpel.2016.2565701.

[14] B. Hu *et al.*, "Deep learning neural networks for heat-flux health condition monitoring method of multi-device power electronics system," in *Proc. IEEE Energy Convers. Congr. Expo. (ECCE)*, Sep. 2019, pp. 3769–3774.

[15] L. Ltd, *Temperature Sensing With Thermcouples and Resistance Thermometers: A Practical Handbook*, 2nd ed. Teddington, U.K.: Labfacility, 1986.

[16] W. M. Rohsenow, J. P. Hstynryy, and Y. I. Cho, *Hand Book of Heat Transfer*, 3rd ed. New York, NY, USA: McGraw-Hill, p. 16.

[17] T. Hjort and L. Glavind, "Optical sensor system and detecting method for an enclosed semiconductor device module," Patent Appl. 20 267 598, Nov. 3, 2011.

[18] E. Baygildina *et al.*, "Application of a heat flux sensor in wind power electronics," *Energies*, vol. 9, no. 6, p. 456, 9456.

[19] R. C. S. B. Allil, M. M. Werneck, B. A. Ribeiro, and F. V. B. de Nazaré, "Application of fiber Bragg grating sensors in power industry," in *Current Trends in Short-and Long-Period Fiber Gratings*. 2013, pp. 133–166.

[20] G.-M. Ma *et al.*, "Distributed partial discharge detection in a power transformer based on phase-shifted FBG," *IEEE Sensors J.*, vol. 18, no. 7, pp. 2788–2795, Apr. 2018.

[21] A. Mohammed and S. Djurovic, "FBG thermal sensing features for hot spot monitoring in random wound electric machine coils," *IEEE Sensors J.*, vol. 17, no. 10, pp. 3058–3067, May 2017.

[22] J.-H. Lee, S.-G. Kim, H.-J. Park, and M. Song, "Investigation of fiber Bragg grating temperature sensor for applications in electric power systems," in *Proc. IEEE 8th Int. Conf. Properties Appl. Dielectric Mater.*, Jun. 2006, pp. 431–434.

[23] Y. J. Rao, "Recent progress in applications of in-fibre Bragg grating sensors," *Opt. Lasers Eng.*, vol. 31, no. 4, pp. 297–324, Apr. 1999.

[24] A. Mohammed and S. Djurovic, "*in-situ* thermal and mechanical fibre optic sensing for in-service electric machinery bearing condition monitoring," in *Proc. IEEE Int. Electr. Mach. Drives Conf. (IEMDC)*, San Diego, CA, USA, May 2019, pp. 37–43.

[25] A. Mohammad and S. Djurovic, "Evaluation of fiber-optic sensing performance for embedded thermal monitoring of electric machinery wound components," in *Proc. 5th Medit. Conf. Embedded Comput. (MECO)*, Jun. 2016, pp. 72–76.

[26] A. Mohammed, J. I. Melecio, and S. Djurovic, "Open-circuit fault detection in stranded PMSM windings using embedded FBG thermal sensors," *IEEE Sensors J.*, vol. 19, no. 9, pp. 3358–3367, May 2019.

[27] M. A. Ismail, N. Tamchek, M. R. A. Hassan, K. D. Dambul, J. Selvaraj, N. A. R. R. Sandoghchi, and F. R. M. Adikan, "A fiber Bragg grating—Bimetal temperature sensor for solar panel inverters," *Sensors*, vol. 11, no. 9, pp. 8665–8673, 2011.

[28] J. P. Bazzo, T. Lukasievicz, M. Vogt, V. De Oliveira, H. J. Kalinowski, and J. C. C. Da Silva, "Monitoring the junction temperature of an IGBT through direct measurement using a fiber Bragg grating," *Proc. SPIE*, vol. 7753, May 2011, Art. no. 77538Q.

[29] J.-L. Zhang, H. You, J. He, X.-J. Xin, and F. Tian, "A fiber Bragg grating sensing system for monitoring IGBT temperature distribution and thermal conduction state of upper surface silicone," *Proc. SPIE*, vol. 10846, Dec. 2018, p. 1084616.

[30] B. Hu *et al.*, "Lifetime consumption of wind turbine power converter in the whole wind speed range," in *Proc. 9th Int. Energy Conf. REMOO*, Hong Kong, Apr. 2019, pp. 16–18.

Anees Mohammed received the M.Sc. degree in electrical power engineering from the University of Newcastle, U.K., in 2010, and the Ph.D. degree in electrical and electronic engineering from the University of Manchester, U.K., in 2019.

He worked as a Research Associate with the Power Conversion Group, University of Manchester and spent four years working as an Assistant Lecturer at Benghazi University, Libya. He currently works for Dyson, U.K. His research interests are in electric machines, drives, and condition monitoring.

Borong Hu (Student Member, IEEE) received the B.Eng. and master's degrees in electrical engineering from Chongqing University, China, in 2014 and 2016, respectively. He is currently pursuing the Ph.D. degree in power electronics with the University of Warwick, U.K. He was a Visiting Scholar with the School of Engineering, University of Warwick, in 2017. His research interests include the reliability, condition monitoring, and operational management of power electronics.

Zedong Hu received the M.Sc. degree in control engineering from the Nanjing University of Science and Technology, Nanjing, China, in 2013, and the Ph.D. degree in the investigation into the high performance of polymer gears from the University of Warwick, Coventry, U.K., in 2018.

She is currently a Research Fellow with the Power Electronics, Application and Technology in Energy Research Group, Warwick, U.K. Her research interests include thermal performance of materials, the reliability of power modules, and monitoring and diagnostics of power electronics.

Siniša Djurović (Member, IEEE) received the Dipl.-Ing. degree in electrical engineering from the University of Montenegro in 2002 and the Ph.D. degree in electrical and electronic engineering from the University of Manchester in 2007. He is currently a Senior Lecturer with the Power Conversion Group, University of Manchester. His research interests are in the area of operation, design, monitoring, and diagnostics of electric machines and drives. He serves as an Editor for the IEEE TRANSACTIONS ON ENERGY CONVERSION and *IET Electric Power Applications*.

Li Ran (Senior Member, IEEE) received the Ph.D. degree in power systems engineering from Chongqing University, Chongqing, China, in 1989. He was a Research Associate with the University of Aberdeen, Aberdeen, U.K., the University of Nottingham, Nottingham, U.K., and the University of Heriot-Watt, Edinburgh, U.K. He became a Lecturer in Power Electronics with Northumbria University, Newcastle upon Tyne, U.K., in 1999 and was seconded to Alstom Power Conversion, Kidsgrove, U.K., in 2001. From 2003 to 2012, he was with Durham University, U.K. He joined the University of Warwick, Coventry, U.K., as a Professor in Power Electronics–Systems, in 2012. His research interest includes the application of power electronics for electric power generation, delivery, and utilization.

Mike Barnes (Senior Member, IEEE) received the B.Eng. degree in engineering and the Ph.D. degree from the University of Warwick, Warwick, U.K., in 1993 and 1998, respectively. He is currently a Professor with the University of Manchester (formerly University of Manchester Institute of Science and Technology), Manchester, U.K. His principal research interests are in power electronics applied to power systems. He is a Fellow of the Institution of Engineering and Technology, U.K. He is an Editor of the IEEE TRANSACTIONS ON ENERGY CONVERSION.

Philip A. Mawby (Senior Member, IEEE) received the B.Sc. and Ph.D. degrees in electronic and electrical engineering from the University of Leeds, Leeds, U.K., in 1983 and 1987, respectively. His Ph.D. degree was focused on GaAs/AlGaAs heterojunction bipolar transistors for high-power radio frequency applications at the GEC Hirst Research Centre, Wembley, U.K. In 2005, he joined the University of Warwick, Coventry, U.K., as the Chair of Power Electronics. He was also with the University of Wales, Swansea, U.K., for 19 years and held the Royal Academy of Engineering Chair for Power Electronics, where he established the Power Electronics Design Center. He has been internationally recognized in the area of power electronics and power device research. He was also involved in the development of device simulation algorithms, as well as optoelectronic and quantum-based device structures. He has authored or coauthored more than 200 journal articles and conference papers. His current research interests include materials for new power devices and the modeling of power devices and circuits. He is a Fellow of the IET and the Institute of Physics.